Preparation of graphene oxide–montmorillonite nanocomposite and its application in multiple-pollutants removal from aqueous solutions

Chengyu Zhang, Jingde Luan, Wei Chen, Xin Ke and Haijun Zhang

ABSTRACT

It is of interest to develop a novel fabrication method of a mineral adsorbent for wastewater treatment to remove the combination of heavy metal ions and refractory organic contaminants. The crosslinking agent stearyl trimethyl ammonium chloride was added into a suspension of montmorillonite and graphene oxide to implement their recombination to fabricated graphene oxide–montmorillonite nanocomposite (GMN). The fabricated nanocomposite was characterized by X-ray diffraction, scanning electron microscopy, Fourier transform infrared spectroscopy, Brunauer–Emmett–Teller analysis and zeta potential. Results indicated that GMN exhibited a honeycomb texture, providing the chemical reaction site for the simultaneous adsorption of Pb^{2+} and *p*-nitrophenol (PNP). Factors including pH value, contact time, contact temperature and GMN dosage in the adsorption process were crucial for both Pb^{2+} adsorption and PNP adsorption. The optimum adsorption capacities of Pb^{2+} and PNP onto GMN were 19.39 $mg \cdot g^{-1}$ and 14.90 $mg \cdot g^{-1}$ under the condition of pH = 6, contact temperature 55 °C, contact time 60 min and GMN dosage 0.10 g, respectively. Data from experimental studies on simultaneous adsorption was well described by the pseudo-second-order model. The implementation of this work shows that GMN is a promising material for application in the simultaneous removal of heavy metal ions and refractory organic contaminants.

Key words | crosslinking modification, graphene oxide–montmorillonite nanocomposite, Pb^{2+}, *p*-nitrophenol, simultaneous removal

Chengyu Zhang
Jingde Luan (corresponding author)
Wei Chen
Xin Ke
Haijun Zhang
College of Energy and Environment,
Shenyang Aerospace University,
No. 37 Daoyi South Avenue, Shenbei New Area,
Shenyang 110136,
China
E-mail: *jdluan@sau.edu.cn*

INTRODUCTION

Inorganic metal ions and organic contaminants are common in industry wastewater, especially heavy metals and refractory organic contaminants (ROCs) (Ömeroğlu Ay *et al.* 2012). These contaminants can exert direct or indirect harm to human health once discharged to the environment (Batool *et al.* 2015). Their combined pollution is a remarkable obstacle to the practical application of wastewater treatment due to their high concentrations, non-biodegradable behavior and the difficulty in treating both together. Nowadays, adsorption stands out from wastewater treatment technologies due to low cost, easy operation and high removal efficiency (Wu *et al.* 2012; Zhang *et al.* 2015). Clay mineral adsorbents have become an alternative to active carbon in recent years, especially montmorillonite (MMt). The sandwich structure of MMt crystal molecule is composed of one central alumina octahedral sheet and two silica tetrahedral sheets (Adrar *et al.* 2017). The interlayer hydrophilicity and cation exchange property of MMt have positive effects on its adsorption performance towards heavy metal ions (Gupta 2009; Yang *et al.* 2016). Meanwhile, organic modification methods have been adopted to convert MMt interlayer hydrophilicity to hydrophobicity, which plays an important role in the improvement of MMt adsorption performance towards organic contaminants (Zhou *et al.* 2015). Graphene oxide (GO) contains both hydrophilic and hydrophobic functional groups, indicating it is a good adsorbent for heavy metal ions and ROCs (Gao 2009; Zhao *et al.* 2011). However, the aggregation behavior of GO in aqueous solution is an adverse factor on its application for pollutant adsorption (Jiang *et al.* 2017). Therefore, it is imperative to improve the dispersion of GO into a single layer to strengthen its adsorption performance (Zhao *et al.* 2015). It is reported that there is no chemical reaction between GO and minerals with surface electronegativity, indicating

doi: 10.2166/wst.2019.046

that it is possible to prepare a suspension of GO and mineral with good dispersity. This suspension can be used to fabricate composite materials with different functions.

GO and MMt were employed to synthesize composite sponge by adding the crossing linker ethylenediamine, which has a positive promotion effect on blood coagulation (Li *et al.* 2016). The solvent method was adopted to prepare GO-MMt nanocomposites, which was characterized as pH-dependent under acid condition (Zhang *et al.* 2015). When agar was introduced into the GO-MMt suspension, the fabricated composites exhibited a good performance for heavy metal removal in low and high pH regions (Cheng *et al.* 2017). Nowadays, GO-MMt based materials as adsorbent have been applied to deal with single-component or binary-component wastewater, such as single or binary heavy metal ions, and organic contaminants (Deng *et al.* 2013; Liu *et al.* 2014; Batool *et al.* 2015; Zhang *et al.* 2015; Liu *et al.* 2016). Although the strong electrostatic attraction between GO and clay minerals inhibited the adsorption of organic contaminants onto GO, the weak electrostatic attraction was convenient for fabricating the GO-MMt nanocomposite adsorbent (Sun *et al.* 2017). As a surface electropositive mineral, MMt modified by cationic surfactant is considered to be a better option to combine with GO for functional material fabrication.

The present work investigated the novel fabrication of GO-MMt nanocomposite using stearyl trimethyl ammonium chloride (STAC) as linkage and the first-time application of the fabricated material for the simultaneous removal of Pb^{2+} and *p*-nitrophenol (PNP) from aqueous solutions. Based on the characterization analysis with X-ray powder diffraction (XRD), scanning electron microscopy (SEM), Fourier transform infrared (FTIR) spectroscopy, and an automatic physical adsorber and zeta potential analyzer, the adsorption mechanism of target contaminants onto GO-MMt nanocomposite and their adsorption competitive behavior have been elucidated in depth.

EXPERIMENT SECTION

Materials

Natural MMt powder reagent was obtained from Gongyi city, Henan province, China. The analytical reagents STAC, lead standard solution and PNP were purchased from China National Pharmaceutical Group Chemical Reagent Co., Ltd. GO powder reagent was purchased from Shanghai Ashine Technology Development Co., Ltd. Deionized water was used for solution preparation, sample cleaning and container cleaning.

Preparation of GO-MMt nanocomposite

Briefly, GO powder (0.1 g) was added into 200 mL of deionized water solution, through the simultaneous treatment of ultrasonic and mechanical stirring for 15 min, to achieve its good dispersion in aqueous solution. Subsequently, 3 g MMt powder was added to the GO dispersion to fabricate a GO-MMt suspension through ultrasonic treatment for 15 min. Then, 1.38 g STAC powder was immersed in this suspension, which was continuously stirred for 120 min. After standing for about 20 min, this suspension was filtered by vacuum to form a filter cake, which was washed three times and placed in a vacuum freeze-drying oven for 15 h to obtain the adsorbent sample.

Materials characterization

XRD patterns were obtained by an X-ray diffractometer (SHIMADZU-7000s) with radiation CuKα under the 2θ range from 2° to 60° at the scanning rate of 2° min^{-1}. The microstructure of GO-MMt nanocomposite was characterized by a field emission scanning electron microscope (JEOL-JSM-7800f, Japan). The change of functional groups was determined by an FTIR spectrometer (Thermo Fisher Nicolet iS10, USA) in the range of spectra between 400 cm^{-1} and 4,000 cm^{-1}. The specific surface area, pore diameter and pore volume of GO-MMt nanocomposite were measured by an automatic physical/chemical adsorption instrument (Quantachrome Autosorb-iQ-C, USA). The potential changes of experimental samples were investigated by a zeta potential analyzer (Malvern-Zetasizer Nano ZS, UK). Pb^{2+} concentration was measured by an inductively coupled plasma mass spectrometer (ICP, PE-Optima-PE8300, USA). The absorbance value of PNP in solution was determined by a UV-vis spectrophotometer (Shanghai Uniko-UV-2100, China) to calculate the PNP concentration.

Adsorption experiments

The lead standard solution was diluted to prepare 100 mg L^{-1} of Pb^{2+} aqueous solution, while PNP was dissolved with deionized water to prepare 150 mg L^{-1} of PNP aqueous solution. Powder samples (0.1 g) of MMt, GO and GO-MMt nanocomposite (GMN) were put into a conical flask containing 20 mL of Pb^{2+}, PNP and their mixed solution, respectively. The conical flask was placed

into a water bath shaker with controlled temperature. Batch experiments were carried out to investigate the effect of the reaction temperature and reaction time on the adsorption performance of GMN. The concentrations of Pb^{2+} and PNP in suspension after adsorption were determined by an ICP and UV-vis spectrophotometer, respectively.

RESULTS AND DISCUSSION

Material characterization

XRD analysis

The diffraction peaks of MMt and GO appeared at 7.26° and 9.80°, indicating that their layer spacing was 12.17 Å and 9.02 Å, respectively (Figure 1). When STAC as linkage was introduced to the suspension containing MMt and GO for GMN fabrication, there was a significant change in the molecular structure and the layer spacing of GMN was 20.83 Å. The increase of the GMN interlayer space was mainly due to the crosslinking recombination of MMt and GO. The increase in the layer spacing had a positive effect on improving the adsorption capacity of contaminants (Kraehenbuehl 1987; Chen *et al.* 2010).

Textural characteristics of GMN adsorbent

The specific surface area, pore volume and pore diameter are the key factors when evaluating the adsorption performance of adsorbent (Ogata *et al.* 2011; Samejima *et al.* 2014). In comparison to MMt, there was a remarkable reduction in the specific surface area of GMN. Compared with MMt and GO, the pore volume of GMN increased by 8.96% and 498.46%, while the pore diameter of GMN increased by 122.06% and 257.40%, respectively (Table 1). It can be seen from the subsequent experiments that the effects of the pore diameter and pore volume on the adsorption capacity were higher than that of the specific surface area. The specific surface area, pore volume and pore diameter of GMN after adsorption of pollutants decreased by 35.45%, 47.04%, and 24.05%, respectively. This phenomenon indicated that adsorption occurred on the surface and in the pore volume and pore diameter between layers.

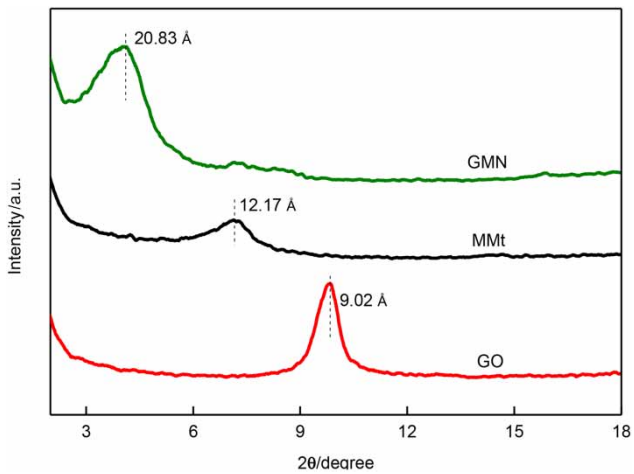

Figure 1 | XRD patterns of MMt, GO and GMN.

Table 1 | The surface property and pore structure of MMt, GO and GMN

Adsorbent	Specific surface area ($m^2\ g^{-1}$)	Pore volume ($cm^3\ g^{-1}$)	Pore diameter (nm)
MMt	80.446	0.357	14.284
GO	28.848	0.065	6.771
GMN before adsorption	35.138	0.389	31.715
GMN after adsorption	22.681	0.206	24.088

SEM and EDS analysis

SEM images indicated that natural MMt was characterized by a lot of blocks with their diameter <1 μm, while GO was characterized by stack curls (Figure 2). When STAC was introduced into the suspension of MMt and GO to prepare nanocomposite, GMN exhibited a honeycomb texture, indicating that STAC successfully acted as a crosslinking agent to realize the recombination of MMt and GO. There were a lot of folds and tiny pores on the honeycomb texture of GMN, which could provide more adsorption sites to enhance its adsorption performance. After the adsorption of target contaminants onto GMN, the folds and tiny pores disappeared, making the honeycomb texture become flat, indicating that the adsorption of target contaminants occurred at the surface and interlayer of GMN.

The energy dispersive spectroscopy (EDS) spectra indicated that the mass percentages of N and O elements increased from 0.00% and 44.94% to 1.07% and 45.61%, respectively, indicating that PNP was successfully adsorbed onto the GMN surface (Figure 3). The mass percentage of Pb element increased from 0% to 0.05% and Na element decreased from 0.17% to 0.06%, which indicated that a small amount of Pb^{2+} was adsorbed on the surface of GMN.

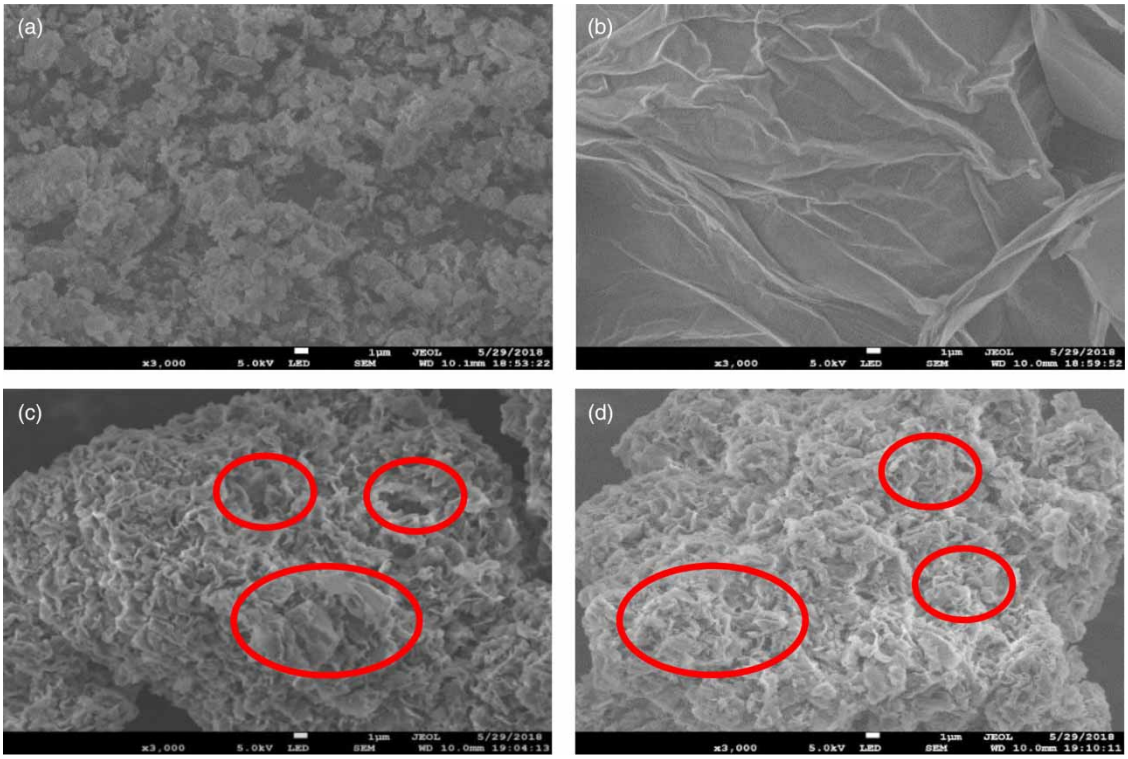

Figure 2 | SEM images of MMt (a), GO (b), GMN (c) and GMN after adsorption (d).

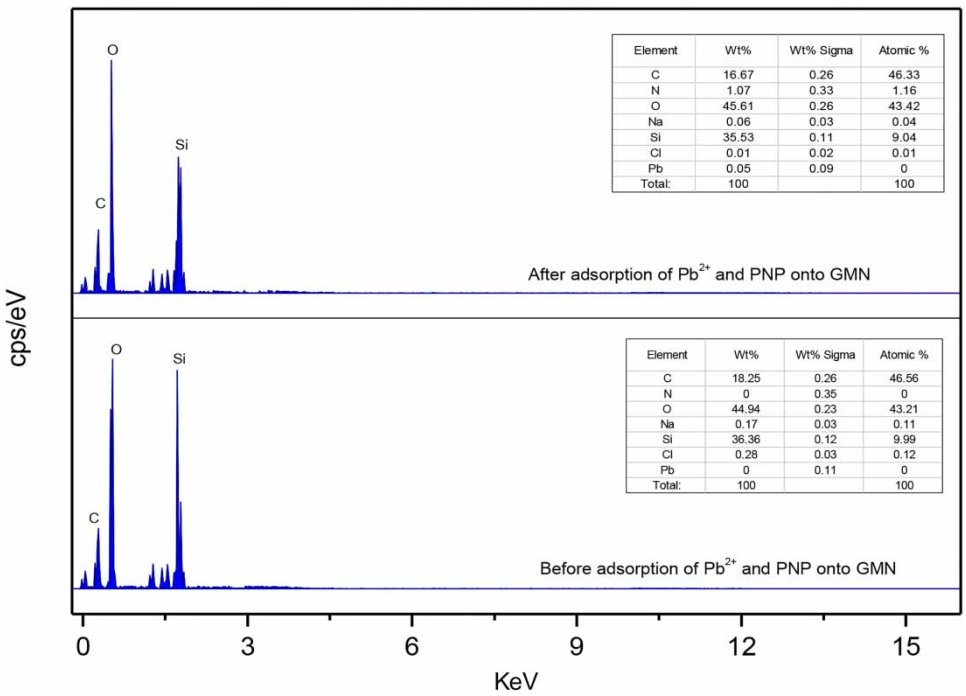

Element	Wt%	Wt% Sigma	Atomic %
C	16.67	0.26	46.33
N	1.07	0.33	1.16
O	45.61	0.26	43.42
Na	0.06	0.03	0.04
Si	35.53	0.11	9.04
Cl	0.01	0.02	0.01
Pb	0.05	0.09	0
Total:	100		100

Element	Wt%	Wt% Sigma	Atomic %
C	18.25	0.26	46.56
N	0	0.35	0
O	44.94	0.23	43.21
Na	0.17	0.03	0.11
Si	36.36	0.12	9.99
Cl	0.28	0.03	0.12
Pb	0	0.11	0
Total:	100		100

Figure 3 | EDS spectra of samples.

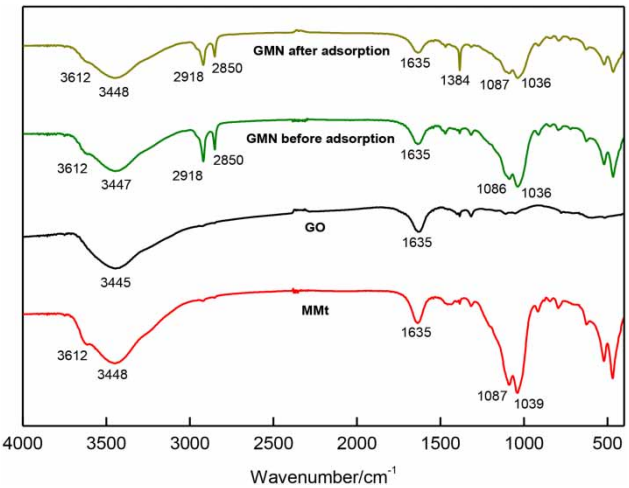

Figure 4 | FTIR spectra of MMt, GO, GMN and GMN after adsorption.

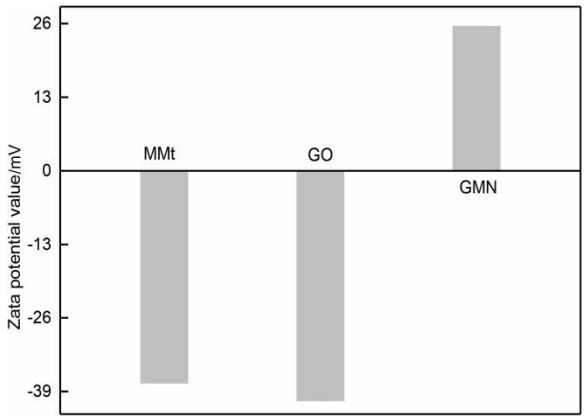

Figure 5 | Zeta potential of MMt, GO and GMN.

FTIR analysis

Clear differences in the peaks between GO, MMt and GMN are seen in Figure 4. In comparison to MMt, there was an occurrence of the absorbance bands centered at 2,850 cm^{-1} and 2,938 cm^{-1}, resulting from C-H symmetric stretching vibration and C-H asymmetric stretching vibration. The results manifested that STAC as linkage was successfully implanted into the MMt interlayer or was arranged in a disordered manner on the MMt surface, indicating that the hydrophilicity of the mineral maybe converted to be hydrophobic. In the case of GMN, the band at 3,612 cm^{-1} corresponded to the stretching vibration of -OH, while the peak at 3,447 cm^{-1} was a consequence of water -OH elongation vibration, and there appeared a weak band at 1,039 cm^{-1}, resulting from Si-O stretching vibration (Liu *et al.* 2013; Lv *et al.* 2015). The presence of these new peaks suggested that MMt successfully combined with GO. When the target contaminants were adsorbed onto GMN, a new peak appeared at 1,384 cm^{-1}, resulting from the cation exchange with Pb^{2+} and the coordination reaction between the active group of GO and contaminants.

Zeta potential analysis

Figure 5 indicates that the surface zeta potential of MMt and GO were −37.5 mV and −40.6 mV, respectively. The surface zeta potential of GMN was 25.5 mV, indicating that STAC successfully acted as the crosslinking agent. The surface negativity of adsorbent is important for static interaction with cations, and the surface electropositivity of adsorbent plays an important role in electrostatic adsorption of anionic pollutants. Zeta potential data have been used to explain the adsorption mechanisms of ionic moieties on the surface (Khaldoun *et al.* 2006; Atta 2016). The zeta potential analysis was consistent with the results of XRD, SEM and FTIR. Obviously, it can be speculated that electrostatic adsorption and the hydrophobicity were beneficial to PNP adsorption. The introduction of STAC did not cause a reduction in the adsorption capacity of Pb^{2+}, indicating that hydrophilic functional groups of GO could provide more active sites to facilitate the adsorption reaction.

Factor analysis on the adsorption of target contaminants onto GMN

Effect of pH value

It has been reported that the flocculent precipitate often appeared due to the combination of heavy metal ions and the hydroxyl radical (OH^-) in high pH aqueous solution (Ijagbemi *et al.* 2009). The adsorption experiment in low pH region was worthwhile to investigate the adsorption performance of GMN on Pb^{2+} and PNP. Preliminary experiments indicated that there was an obvious occurrence of the flocculent precipitate when pH value of prepared solution exceeded 6.3. Therefore, the effect of low pH on adsorption capacity of target contaminants onto GMN was investigated under the condition of the reaction temperature 25 °C and the reaction time 120 min. Figure 6(a) indicates that there was a significant increase in the adsorption capacity of Pb^{2+} onto GMN from 1.86 $mg{\cdot}g^{-1}$ to 19.94 $mg{\cdot}g^{-1}$, indicating that the removal efficiency of Pb^{2+} went up by 90.41% in the range of pH value from 2 to 6. This phenomenon was related to the adsorptive sites and electrostatic attraction. In low pH solution, hydrogen ion has obvious advantages in the competition for adsorption sites

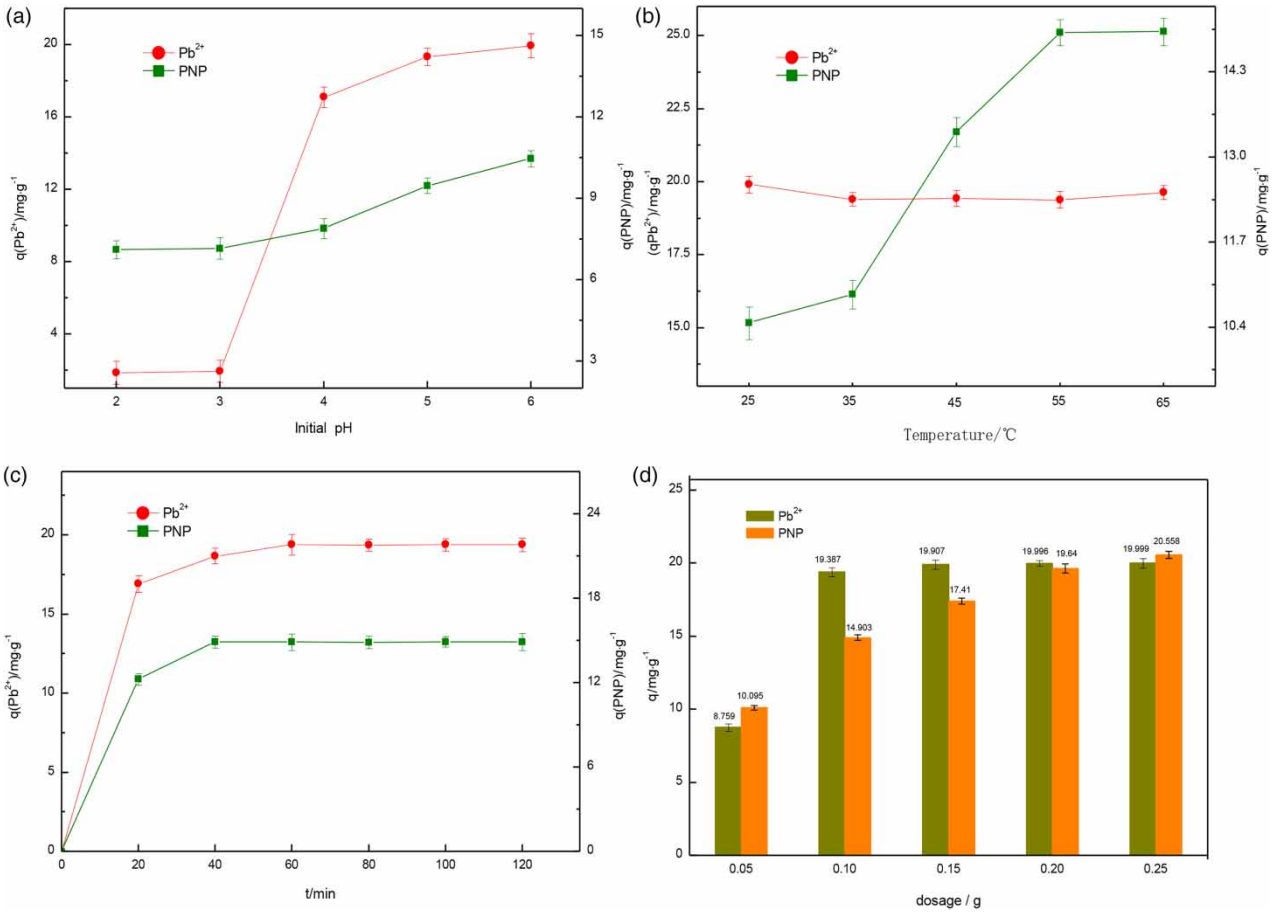

Figure 6 | Simultaneous adsorption of Pb^{2+} and PNP by GMN under different conditions.

with heavy metal ions (Cui *et al.* 2012; Ravikumar *et al.* 2014). Meanwhile, the electropositive surface of carboxyl group and hydroxyl group caused by the strong protonation produced electrostatic repulsion on Pb^{2+} (Fan *et al.* 2012). The adsorption capacity of PNP onto GMN increased from 7.11 $mg \cdot g^{-1}$ to 10.46 $mg \cdot g^{-1}$, indicating that PNP removal efficiency went up by 11.17% in the pH ranging from 2 to 6. The results might be related to GO and the interlayer hydrophobicity of MMt.

Effect of contact temperature

The effect of contact temperature on the simultaneous removal of Pb^{2+} and PNP was investigated at the condition of contact time 120 min and pH = 6. When the contact temperature was in the range from 25 °C to 65 °C, there was a remarkable increase in PNP adsorption capacity onto GMN from 10.46 $mg \cdot g^{-1}$ to 14.91 $mg \cdot g^{-1}$, while Pb^{2+} adsorption capacity onto GMN fluctuated slightly between 19.39 $mg \cdot g^{-1}$ and 19.91 $mg \cdot g^{-1}$ in Figure 6(b). In comparison to Pb^{2+} adsorption, there was an obvious sensitivity of GMN for PNP adsorption. Overall, the total adsorption capacity of Pb^{2+} and PNP was higher than 34 $mg \cdot g^{-1}$ when contact time exceeded 55 °C.

Effect of contact time

The effect of contact time on the simultaneous removal of Pb^{2+} and PNP was investigated at the condition of contact temperature 55 °C and pH = 6. It was clearly seen that the adsorptions of Pb^{2+} and PNP were fairly rapid on GMN to reach equilibrium within 60 min and 40 min, respectively (Figure 6(c)).

Effect of GMN dosage

The effect of GMN dosage on the simultaneous removal of Pb^{2+} and PNP was investigated at the condition of pH = 6, contact temperature 55 °C and contact time 60 min. Figure 6(d) indicates that the adsorption capacities of

Pb^{2+} and PNP onto GMN were 8.76 $mg \cdot g^{-1}$ and 10.10 $mg \cdot g^{-1}$, respectively. The adsorptions of Pb^{2+} and PNP were fairly rapid onto GMN to reach 19.39 $mg \cdot g^{-1}$ and 14.90 $mg \cdot g^{-1}$, respectively, when GMN dosage increased from 0.05 g to 0.10 g. The continuous increase of GMN dosage presented a slightly higher adsorption capacity of Pb^{2+}. However, PNP adsorption on GMN still presented a rapid increase. The results indicated that the adsorption of Pb^{2+} in aqueous solution was close to saturation with 0.10 g GMN dosage. The continuous increase in PNP adsorption was ascribed to the higher concentration of GO in GMN dosage.

Comparison of the maximum adsorption capacity for Pb^{2+}

We compared the present GMN's maximum Pb^{2+} adsorption capacity in the combined-pollutant system with the results for the adsorption of Pb^{2+} as a single pollutant by other materials. Table 2 reveals that GMN's simultaneous adsorption of Pb^{2+} was 27.12 $mg \cdot g^{-1}$ and single adsorption for Pb^{2+} by other materials is high. Our research focuses more on the synchronous adsorption of heavy metal ions and anionic organics onto GMN, and we hope that our research can provide useful information for the treatment of wastewater with compound pollutants.

Adsorption isotherm analysis

Langmuir and Freundlich adsorption isotherm models were adopted to gain insight on the adsorption performance of MMt, GO and GMN for Pb^{2+} and PNP. These models with details are given in the Supporting Information (available with the online version of this paper). The adsorption capacity and adsorption parameters are shown in Figure 7 and Table S1 (available online). The adsorption capacity of GMN for PNP went up by 80.94% compared with GO, indicating that the agglomeration effect of GO in solution was successfully prevented. Although there was a slight reduction in the adsorption capacity of Pb^{2+} due to the electrostatic repulsion caused by the surface electropositivity, GMN still maintained a high adsorption capacity. The Langmuir adsorption isotherm simulation also showed that the maximum adsorption capacity of GMN for PNP was 112.09% and 183.11% higher than that of MMt and GO, respectively. Obviously, the significant improvement in PNP adsorption onto GMN resulted from the hydrophobic groups on GO. According to the value of R_L, the isothermal adsorption line can be divided into non-preferential adsorption ($R_L > 1$), linear adsorption ($R_L = 1$), preferential adsorption ($0 < R_L < 1$) and irreversible adsorption ($R_L = 0$) (Alslaibi *et al.* 2013; Aziz *et al.* 2013; Sivasankari & Arulanantham 2014). Because all the R_L values were between 0 and 1, the adsorption process was preferential adsorption. Freundlich adsorption isotherm models indicated that the adsorption capacity of Pb^{2+} and PNP onto GMN was quite different from the actual experimental data. The degree of difficulty of the adsorption process can be judged by the value of the constant 1/n. The Freundlich constant 1/n was between 0.1 and 0.5 indicating that the adsorption of pollutants by the adsorbent was relatively easy to carry on (Nadia & F Handan 2004; Vinod *et al.* 2010). As seen from Table S1, the Langmuir model was a better fit ($r^2 > 0.99$) than the Freundlich adsorption isotherm model.

Adsorption kinetics simulation analysis

Adsorption kinetics simulation was used to describe the adsorption mechanism of GMN for the simultaneous removal of Pb^{2+} and PNP in aqueous solution (Figure 8). Five models with details (pseudo-first-order model, pseudo-second-order model, intraparticle diffusion model, Bangham model and Elovich model) in this work are given in the

Table 2 | Comparison of the maximum adsorption capacity for Pb^{2+}

Adsorbent	pH	Single or combined adsorption	Maximum adsorption capacity, q_{max}($mg \cdot g^{-1}$)	References
Mesoporous silica nano-adsorbent	5.2	Single	169.34	Khaleque (2015)
Ash and Fe nanoparticles loaded ash	6	Single	588.2 and 833.3	Ghasemi *et al.* (2014b)
SDS-AZS nano-composite	6	Single	21.01	Naushad (2014)
Fig sawdust activated carbon	4	Single	80.645	Ghasemi *et al.* (2014a)
Ti(IV) iodovanadate cation exchanger	6	Single	63.29	Naushad *et al.* (2015)
GMN	6	Combined	27.12	Present study

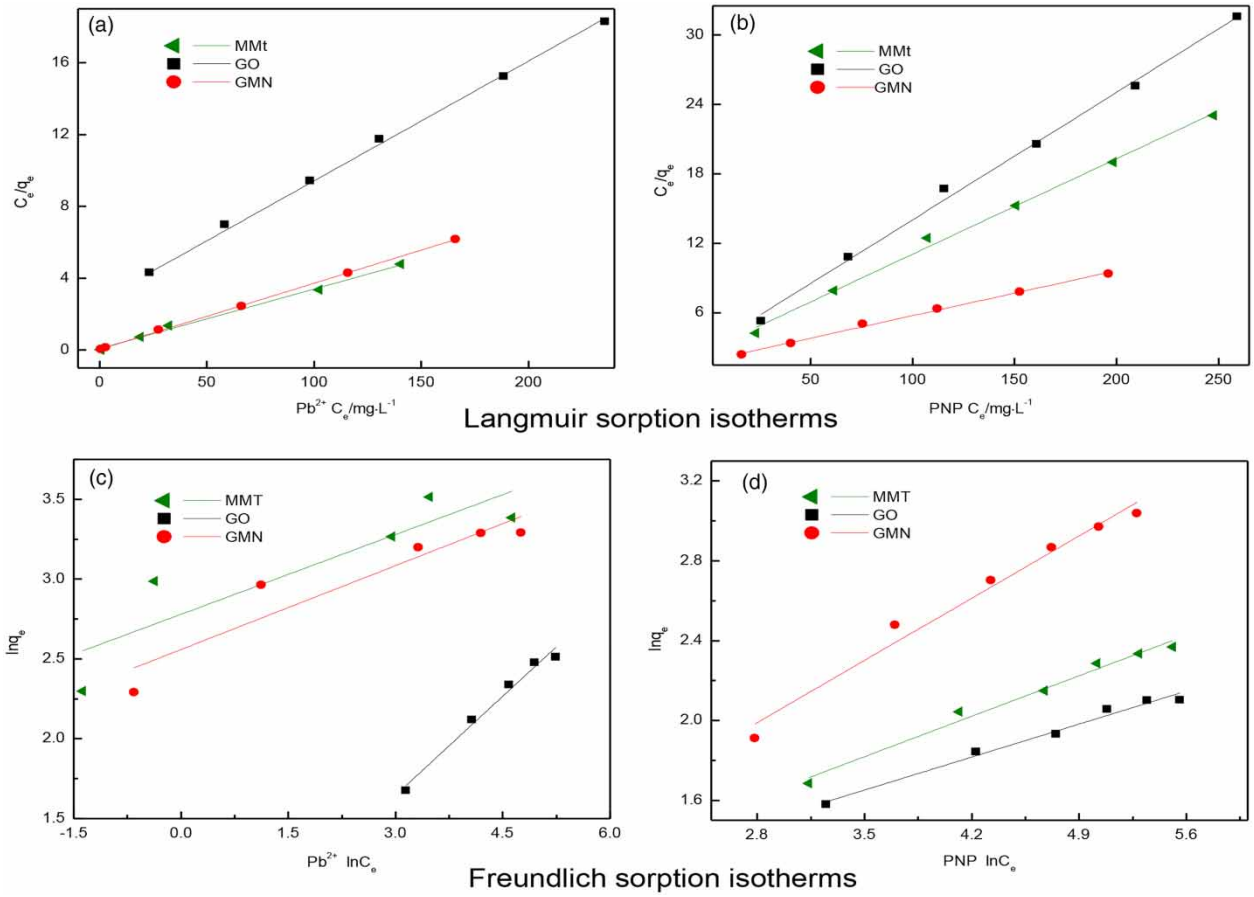

Figure 7 | Langmuir and Freundlich sorption isotherms analysis on the simultaneous adsorption of Pb^{2+} and PNP.

Supporting Information. The rate constants, adsorption capacity and correlation coefficients (R^2) are three key factors to carry out the evaluation of adsorption kinetic models. The pseudo-second-order model provided the best correlation to experimental data, shown by the highest R^2 values and the greatest similarity between experimental and equilibrium adsorption capacities for this model. (Table S2, available online), indicating that chemical adsorption was the possible restriction that formed coordination compound adsorption and hydrophobic bond adsorption.

The intraparticle diffusion model was considered as an efficient method to the further elaborate the diffusion mechanisms and identify the possible rate controlling procedure (Chen *et al.* 2016). The plot of q_t versus $t^{1/2}$ indicated that there were three stages in the adsorption process. Specifically, the first stage could be ascribed to the molecular diffusion of adsorbate from water surface to the adsorbent surface. The second stage could be attributed to the diffusion of adsorbates in the particles of adsorbent. Figure 8(c) shows that the linear part does not pass through the origin, indicating that the intraparticle diffusion was not the only step controlling the adsorption process. Moreover, there was also the presence of material exchange and other chemical reactions. The third stage indicated that the intraparticle diffusion of target contaminants on GMN diminished gradually after the equilibrium of diffusion adsorption was reached.

The Bangham model indicates that the diffusion within the adsorbent is the control step of the adsorption rate. When the correlation coefficient $R^2 > 0.99$, it indicates that the pore diffusion model can better represent the actual adsorption. The Elovich model is used to describe the adsorption behavior of pollutants on a heterogeneous solid surface. The Elovich model does not have a clear assumption of the adsorption mechanism, but it can describe the kinetics of the chemical adsorption process. The two models had a relatively poor fit to the experimental data (Figure 8 and Table S2). Therefore, these two adsorption kinetic models did not describe the process of adsorption of Pb^{2+} and PNP onto GMN very well.

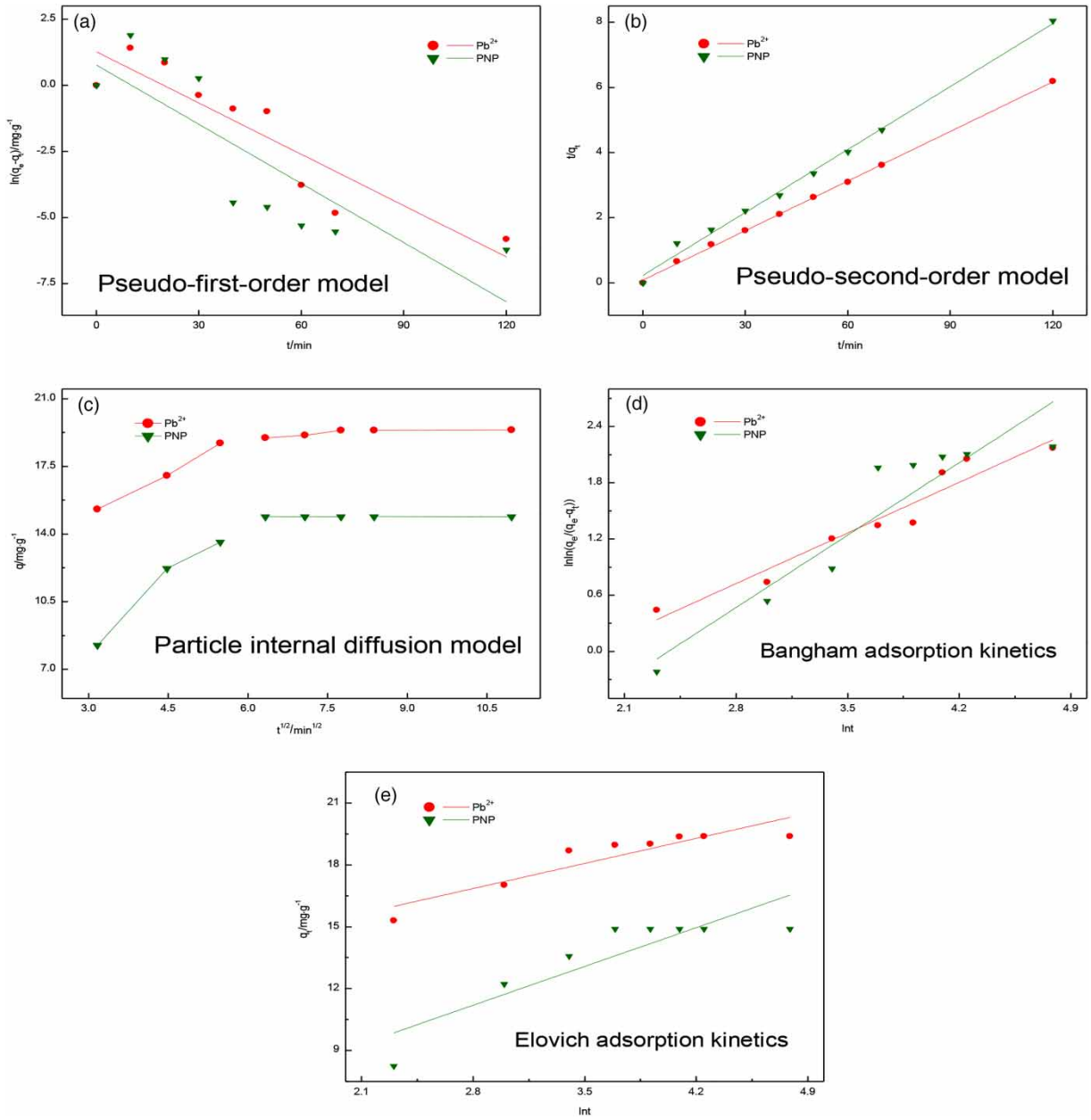

Figure 8 | Different adsorption kinetics models.

CONCLUSIONS

The crosslinking agent STAC was added into a suspension containing MMt and GO to fabricate GMN. The resulting GMN was used to carry out the simultaneous removal of Pb^{2+} and PNP from aqueous solution. The adsorption experiments were conducted under conditions that differed in pH value, contact temperature, contact time and GMN dosage. The experimental results indicated that the simultaneous adsorption capacities of Pb^{2+} and PNP onto GMN were 19.39 mg·g^{-1} and 14.90 mg·g^{-1}, respectively, under the condition of pH = 6, contact temperature 55 °C, contact time 60 min and GMN dosage 0.1 g. Material characterization suggested that the honeycomb texture of GMN provided the chemical reaction sites for Pb^{2+} and PNP in the simultaneous adsorption. The adsorption kinetics of target contaminants onto GMN was well described by the pseudo-second-order model, while the simultaneous

adsorption rate was dominated by the intraparticle diffusion process. Overall, GMN is a promising material for application in the simultaneous removal of heavy metal ions and the electronegative organic pollutants from aqueous solution.

SUPPORTING INFORMATION

The supplementary data associated with this article (available with the online version) contains the mathematical expressions and variable definitions of the Langmuir adsorption isotherm model, pseudo-first-order model, pseudo-second-order model, intraparticle diffusion model, Bangham adsorption kinetic model and Elovich adsorption kinetic model. The supplementary also includes the comparison of GMN and GO in their adsorption performance, the adsorbent regeneration, and the tables for adsorption isotherm parameters and kinetics parameters.

AUTHOR CONTRIBUTIONS

The manuscript was written through contributions of all authors. All authors have given approval to the final version of the manuscript.

NOTES

The authors declare no competing financial interest.

ACKNOWLEDGEMENTS

This work was financially supported by the Major Science and Technology Program for Water Pollution Control and Treatment (grant number 2012ZX07202-004-02) and Liaoning Provincial Natural Science Foundation of China (grant number 20180510024).

REFERENCES

Adrar, S., Habi, A., Ajji, A. & Grohens, Y. 2017 Combined effect of epoxy functionalized graphene and organomontmorillonites on the morphology, rheological and thermal properties of poly (butylenes adipate-*co*-terephtalate) with or without a compatibilizer. *Applied Clay Science* **146**, 306–315.

Alslaibi, T. M., Abustan, I., Ahmad, M. A. & Foul, A. A. 2013 Cadmium removal from aqueous solution using microwaved olive stone activated carbon. *Journal of Environmental Chemical Engineering* **1** (3), 589–599.

Atta, A. M. 2016 Effect of zeta potential of exfoliated amphiphilic montmorillonite nanogels on removal efficiencies of cationic dye water pollutant. *International Journal of Electrochemical Science* **11** (5), 3786–3802.

Aziz, A. S. A., Manaf, L. A., Man, H. C. & Kumar, N. S. 2013 Kinetic modeling and isotherm studies for copper(II) adsorption onto palm oil boiler mill fly ash (POFA) as a natural low-cost adsorbent. *Bioresources* **9** (1), 336–356.

Batool, S., Akib, S., Ahmad, M., Balkhair, K. S. & Ashraf, M. A. 2015 Study of modern nano enhanced techniques for removal of dyes and metals. *Journal of Nanomaterials* **2014** (21), 1–20.

Chen, D. M., Chen, J., Wang, X. M., Luan, X. L., Ji, H. P. & Xu, F. 2010 Adsorption of methylene blue from aqueous solution by anionic surfactant modified montmorillonite. *Advanced Materials Research* **178**, 29–34.

Chen, W., Zhang, X., Mamadiev, M., Zhao, C., Wang, Z. & Xu, H. 2016 Synthesis of interstratified graphene/montmorillonite composite material through organics-pillared, delamination and co-stacking and its application in hexavalent chromium removal from aqueous solution. *Advanced Powder Technology* **28** (2), 521–533.

Cheng, W., Ding, C., Nie, X., Duan, T. & Ding, R. 2017 Fabrication of 3D macroscopic graphene oxide composites supported by montmorillonite for efficient U(VI) wastewater purification. *ACS Sustainable Chemistry & Engineering* **5** (6), 5503–5511.

Cui, H., Yan, Q., Li, Q., Zhang, Q. & Zhai, J. 2012 Adsorption of aqueous Hg(II) by a polyaniline/attapulgite composite. *Chemical Engineering Journal* **211–212** (22), 216–223.

Deng, J. H., Zhang, X. R., Zeng, G. M., Gong, J. L., Niu, Q. Y. & Liang, J. 2013 Simultaneous removal of Cd(II) and ionic dyes from aqueous solution using magnetic graphene oxide nanocomposite as an adsorbent. *Chemical Engineering Journal* **226** (8), 189–200.

Fan, L., Zhang, Y., Luo, C., Lu, F., Qiu, H. & Sun, M. 2012 Synthesis and characterization of magnetic β-cyclodextrin-chitosan nanoparticles as nano-adsorbents for removal of methyl blue. *International Journal of Biological Macromolecules* **50** (2), 444–450.

Gao, W. 2009 The chemistry of graphene oxide. *Chemical Society Reviews* **39** (1), 228–240.

Ghasemi, M., Naushad, M., Ghasemi, N. & Khosravi-Fard, Y. 2014a A novel agricultural waste based adsorbent for the removal of Pb(II) from aqueous solution: kinetics, equilibrium and thermodynamic studies. *Journal of Industrial & Engineering Chemistry* **20** (2), 454–461.

Ghasemi, M., Naushad, M., Ghasemi, N. & Khosravifard, Y. 2014b Adsorption of Pb(II) from aqueous solution using new adsorbents prepared from agricultural waste: adsorption isotherm and kinetic studies. *Journal of Industrial & Engineering Chemistry* **20** (4), 2193–2199.

Gupta, V. K. 2009 Application of low-cost adsorbents for dye removal – a review. *Journal of Environmental Management* **90** (8), 2313–2342.

Ijagbemi, C. O., Mihwa, B. & Dongsu, K. 2009 Montmorillonite surface properties and sorption characteristics for heavy metal removal from aqueous solutions. *Journal of Hazardous Materials* **166** (1), 538–546.

Jiang, Y., Raliya, R., Liao, P., Biswas, P. & Fortner, J. D. 2017 Graphene oxides in water: assessing stability as a function of material and natural organic matter properties. *Environmental Science Nano* **4** (7), 1484–1493.

Khaldoun, A., Wegdam, G. H., Eiser, E., Kerkeb, M. L., Duran, J. D. G., González-Caballero, F. & Bonn, D. 2006 Influence of heavy metals adsorption on the surface-energy properties of fluorinated montmorillonite clays 'Rassoul'. *Colloids & Surfaces A Physicochemical & Engineering Aspects* **290** (1), 1–6.

Khaleque, M. A. 2015 Large-pore diameter nano-adsorbent and its application for rapid lead(II) detection and removal from aqueous media. *Chemical Engineering Journal* **273**, 286–295.

Kraehenbuehl, F. 1987 Study of the water-bentonite system by vapour adsorption, immersion calorimetry and X-ray techniques: I. micropore volumes and internal surface areas, following Dubinin's theory. *Clay Minerals* **22** (1), 1–9.

Li, G., Quan, K., Liang, Y., Li, T., Yuan, Q., Tao, L., Xie, Q. & Wang, X. 2016 Graphene-montmorillonite composite sponge for safe and effective hemostasis. *ACS Applied Materials & Interfaces* **8** (51), 35071–35080.

Liu, D., Yuan, P., Liu, H., Cai, J., Tan, D., He, H., Zhu, J. & Chen, T. 2013 Quantitative characterization of the solid acidity of montmorillonite using combined FTIR and TPD based on the NH_3 adsorption system. *Applied Clay Science* **80–81** (8), 407–412.

Liu, L., Zhang, Y., He, Y., Xie, Y., Huang, L., Tan, S. & Cai, X. 2014 Preparation of montmorillonite-pillared graphene oxide with increased single- and co-adsorption towards lead ions and methylene blue. *RSC Advances* **5** (6), 3965–3973.

Liu, C., Wu, P., Zhu, Y. & Tran, L. 2016 Simultaneous adsorption of Cd^{2+} and BPA on amphoteric surfactant activated montmorillonite. *Chemosphere* **144**, 1026–1032.

Lv, G., Li, Z., Jiang, W. T., Chang, P. H. & Liao, L. 2015 Interlayer configuration of ionic liquids in a Ca-montmorillonite as evidenced by FTIR, TG-DTG, and XRD analyses. *Materials Chemistry & Physics* **162**, 417–424.

Nadia, R. & F Handan, T. 2004 Removal of phenol from aqueous solutions by adsorption. *Journal of Environmental Management* **70** (2), 157–164.

Naushad, M. 2014 Surfactant assisted nano-composite cation exchanger: development, characterization and applications for the removal of toxic Pb^{2+} from aqueous medium. *Chemical Engineering Journal* **235** (1), 100–108.

Naushad, M., ALOthman, Z. A., Awual, R. M., Alam, M. M. & Eldesoky, G. E. 2015 Adsorption kinetics, isotherms, and thermodynamic studies for the adsorption of Pb^{2+} and Hg^{2+} metal ions from aqueous medium using Ti(IV) iodovanadate cation exchanger. *Ionics* **21** (8), 2237–2245.

Ogata, F., Tominaga, H., Kangawa, M., Inoue, K. & Kawasaki, N. 2011 Properties of carbonaceous material produced from cotton and its dye adsorption capabilities. *e-Journal of Surface Science and Nanotechnology* **9**, 380–385.

Ömeroğlu Ay, Ç., Özcan, A. S., Erdoğan, Y. & Özcan, A. 2012 Characterization of *Punica granatum* L. peels and quantitatively determination of its biosorption behavior towards lead(II) ions and Acid Blue 40. *Colloids and Surfaces B: Biointerfaces* **100**, 197–204.

Ravikumar, L., Kalaivani, S., Vidhyadevi, T., Murugasen, A., Kirupha, S. D. & Sivanesan, S. 2014 Synthesis, characterization and metal ion adsorption studies on novel aromatic poly(azomethine amide)s containing thiourea groups. *Open Journal of Polymer Chemistry* **4** (1), 1–11.

Samejima, T., Soh, Y. & Yano, T. 2014 Specific surface area and specific pore volume distribution of tobacco. *Journal of the Agricultural Chemical Society of Japan* **41** (6), 983–988.

Sivasankari, C. & Arulanantham, A. 2014 Evaluation of polymer-agglomerated granular tri-calcium phosphate for fluoride removal from drinking water. *Indian Journal of Chemical Technology* **21** (1), 70–77.

Sun, W., Wang, C., Pan, W., Li, S. & Chen, B. 2017 Effects of natural minerals on the adsorption of 17β-estradiol and bisphenol A on graphene oxide and reduced graphene oxide. *Environmental Science Nano* **4** (6), 1377–1388.

Vinod, K. N., Gowda, K. N. & Sudhakar, R. 2010 Extraction, identification and adsorption-kinetic studies of a natural color component from *G. sepium*. *Natural Science* **2** (5), 469–475.

Wu, P., Dai, Y., Long, H., Zhu, N., Li, P., Wu, J. & Dang, Z. 2012 Characterization of organo-montmorillonites and comparison for Sr(II) removal: equilibrium and kinetic studies. *Chemical Engineering Journal* **191** (19), 288–296.

Yang, S., Wu, P., Chen, L., Li, L., Huang, Z., Liu, S. & Li, L. 2016 A facile method to fabricate N-doped graphene-like carbon as efficient electrocatalyst using spent montmorillonite. *Applied Clay Science* **132–133**, 731–738.

Zhang, Z., Luo, H. J., Jiang, X., Jiang, Z. & Yang, C. 2015 Synthesis of reduced graphene oxide-montmorillonite nanocomposite and its application in hexavalent chromium removal from aqueous solutions. *RSC Advances* **5** (59), 47408–47417.

Zhao, G., Li, J., Ren, X., Chen, C. & Wang, X. 2011 Few-layered graphene oxide nanosheets as superior sorbents for heavy metal ion pollution management. *Environmental Science & Technology* **45** (24), 10454–10462.

Zhao, J., Liu, F., Wang, Z., Cao, X. & Xing, B. 2015 Heteroaggregation of graphene oxide with minerals in aqueous phase. *Environmental Science & Technology* **49** (5), 2849–2857.

Zhou, Q., Zhu, R., Parker, S., Zhu, J., He, H. & Molinari, M. 2015 Modelling the effects of surfactant loading level on the sorption of organic contaminants on organoclays. *RSC Advances* **5** (58), 47022–47030.

First received 27 September 2018; accepted in revised form 21 January 2019. Available online 28 January 2019